Research Square

Preprints are preliminary reports that have not undergone peer review.
They should not be considered conclusive, used to inform clinical practice,
or referenced by the media as validated information.

Airborne observations of fast-evolving ocean submesoscale turbulence

Hector Torres

Hector.Torres.Gutierrez@jpl.nasa.gov

JPL/Caltech

Ernesto Rodriguez

JPL/Caltech

Alexander Wineteer

JPL/Caltech

Patrice Klein

Caltech https://orcid.org/0000-0002-3089-3896

Andrew Thompson

California Institute of Technology https://orcid.org/0000-0003-0322-4811

Jörn Callies

California Institute of Technology https://orcid.org/0000-0002-2278-2811

Eric D'Asaro

University of Washington https://orcid.org/0000-0002-8453-854X

Dragana Perkovic-Martin

JPL/Caltech

John Farrar

WHOI https://orcid.org/0000-0003-3495-1990

Federica Polverari

JPL/Caltech

Ruzbeh Akbar

JPL/Caltech

Article

Keywords: Ocean cross-scale interactions, submesoscale turbulence, Doppler Scatterometer

Posted Date: June 28th, 2024

DOI: https://doi.org/10.21203/rs.3.rs-4421539/v1

License: This work is licensed under a Creative Commons Attribution 4.0 International License.
Read Full License

Additional Declarations: There is **NO** Competing Interest.

Version of Record: A version of this preprint was published at Communications Earth & Environment on December 19th, 2024. See the published version at https://doi.org/10.1038/s43247-024-01917-3.

Airborne observations of fast-evolving ocean submesoscale turbulence

Hector S. Torres[1*], Ernesto Rodriguez[1], Alexander Wineteer[1], Patrice Klein[1,2,3], Andrew F. Thompson[2], Jörn Callies[2], Eric D'Asaro[4], Dragana Perkovic-Martin[1], J. Thomas Farrar[5], Federica Polverari[1], Ruzbeh Akbar[1]

[1*]Jet Propulsion Laboratory, California Institute of Technology, Pasadena, 91109, CA, USA.
[2]Department of Environmental Science and Engineering, California Institute of Technology, Pasadena, CA, USA.
[3]Laboratoire de Météorologie Dynamique, Ecole Normale Supérieure, Paris, France.
[4]Applied Physics Laboratory, University of Washington, Seattle, WA, USA.
[5]Woods Hole Oceanographic Institution,Woods Hole, MA, USA.

*Corresponding author(s). E-mail(s): hector.torres.gutierrez@jpl.nasa.gov;
Contributing authors: ernesto.rodriguez@jpl.nasa.gov; alexander.g.wineteer@jpl.nasa.gov; pklein@caltech.edu; andrewt@caltech.edu; jcallies@caltech.edu; dasaro@apl.washington.edu; dragana.perkovic@jpl.nasa.gov; jfarrar@whoi.edu; federica.polverari@jpl.nasa.gov; ruzbeh.akbar@jpl.nasa.gov;

Abstract

Ocean images collected by astronauts onboard the Apollo spacecraft more than 50 years ago revealed for the first time a large number of ocean eddies, with a size between 1 and 20 km. Since then, satellite infrared, ocean color, sun glitter and synthetic aperture radar images, with high spatial resolution, have confirmed the ubiquitous presence of these small eddies in all oceans. However, observing the dynamical characteristics and evolution of these eddies has remained challenging. An experiment was recently carried out in the California Current system using the new airborne Doppler Scatterometer (NASA-JPL DopplerScatt)

instrument that observes surface velocities. With DopplerScatt, we mapped a 30 km × 100 km domain over multiple days to unveil numerous 1–20 km ocean eddies, called submesoscale eddies, that evolve over a period of a few hours. The strong interactions between eddies generate horizontal velocity divergence, implying vertical velocities reaching 250 m day^{-1} at 40 m depth. The velocity field also produces horizontal dispersion of particles over a distance of 50 km within 12 hours, which rapidly fills the turbulent eddy field. These observations suggest that submesoscale ocean turbulence may profoundly affect the vertical transport of heat, carbon, and important climatic gases between the atmosphere and the ocean interior, as well as the horizontal dispersion of tracers and particles. As such, submesoscale ocean eddies are a critical element of Earth's climate system.

Keywords: Ocean cross-scale interactions, submesoscale turbulence, Doppler Scatterometer

1 Introduction

In 2000, Walter Munk [1] analyzed more than 500 photographs collected by astronauts on board the Apollo and Space Shuttle missions. These photographs are sun glitter images (reflectance of the sun on the sea surface) that revealed a high density of interconnected eddies with a size ranging from 1 to 20 km (Fig. 1a). Estimation of the sharp break of ships' wakes present on these images indicated that the velocity associated with these eddies can reach 0.2 m s^{-1} and a horizontal shear of 10^{-3} s^{-1} [1]. Since then, the ubiquitous existence of such interconnected, small-scale eddies, which Paul Sculler-Power (the only astronaut oceanographer) called in 1986 submesoscale eddies, has been confirmed by satellite infrared, ocean color, sun glitter, and synthetic aperture radar images. A recent study based on ocean color satellite images emphasizes that these cyclonic and anticyclonic submesoscale eddies are present in all seasons with a slight predominance of cyclonic eddies [2]. Several mechanisms have been proposed to explain the emergence of these submesoscale eddies, such are gravity convection, horizontal current shear, mixed-layer instabilities, wind intermittency, and frontal instability [3–9], all of which are relevant for the upper ocean[10].

The magnitudes of the horizontal velocities and horizontal shears estimated by ref [1] have been confirmed by a few recent *in situ* experiments focusing on isolated eddies[3, 6]. Recent studies [9, 11] suggest these large values of velocities and shears may result from the mutual interactions between eddies, leading to a vigorous vertical circulation in the upper oceanic layers that connects the ocean interior to the atmosphere. It has remained challenging so far, however, to assess the processes underlying the submesoscale interactions and the resulting vertical circulation from in situ observations, because the rapidly evolving circulation requires observations spanning a wide range of spatial scales that can evolve over a period of a day.

Here, we report on progress toward meeting this challenge using an airborne Doppler Scatterometer instrument (NASA-JPL DopplerScatt) [12] deployed during the 2022

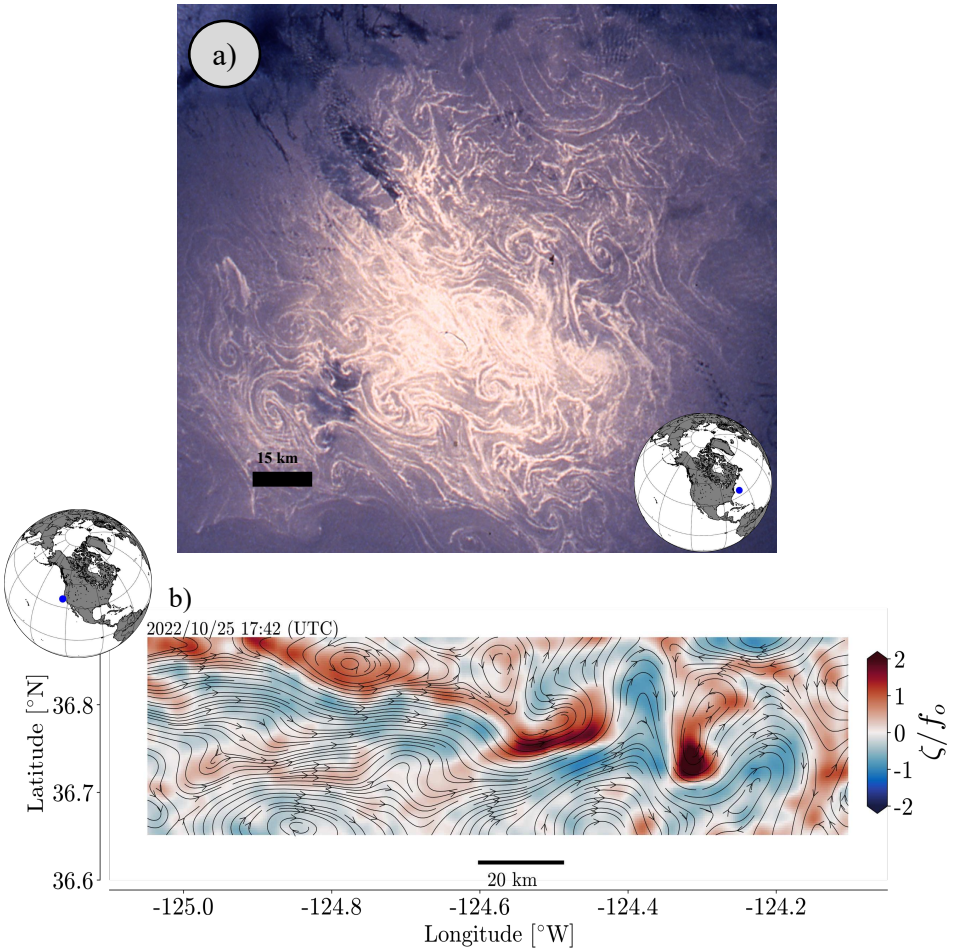


Fig. 1: **A view of the ocean turbulence from space and from airborne observations.** a) Photograph taken off the northeastern seaboard of the United States in October 1984 during the Space Shuttle mission STS-41G [1]. The photo shows spiral eddies in the Gulf Stream highlighted in the Sun glitter. b) DopplerScatt relative vorticity (shading) in the S-MODE area in the California Current System. Black contours are streamlines of the rotational component of the high-pass surface velocity field.

S-MODE campaign [13] (Extended Data Fig. 1b,c,d,e). DopplerScatt measured the ocean surface velocity over a 30 km × 100 km domain with a spatial resolution of 200 m (see Methods) and an accuracy better than 0.04 m s^{-1} over a period of less than 3 hours. These observations reveal multiple submesoscale eddies embedded in a mesoscale eddy field, as shown in Fig. 1b and Extended Data Fig.1, consisting of numerous submesoscale cyclones and anticyclones. The submesoscale eddies evolve over time scales less than 12 hours, each one having vorticity (the spin of the eddies)

and divergence (associated with vertical velocity) of order $f = 10 \times 10^{-5}$ s^{-1}, the local planetary vorticity (Fig. 2). We analyze a subset of the DopplerScatt data to characterize the eddy interactions and their relationship with divergence and horizontal dispersion.

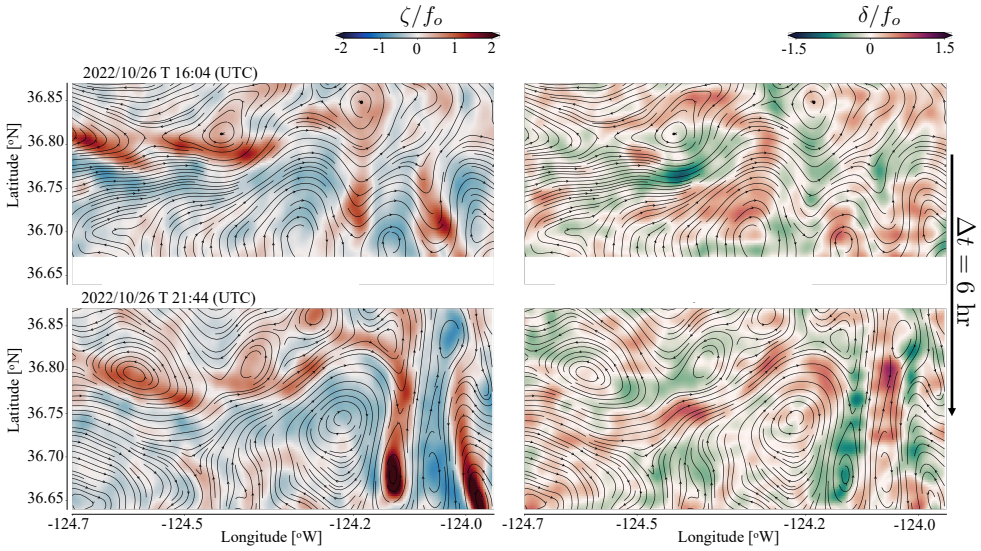


Fig. 2: **Time evolution of surface vorticity and divergence** computed at 2-km scale from DopplerScatt observations on October 26th, 2022 at 16:04 UTC (top panels) and 21:44 UTC (bottom panels). These times represent the average time of each map. Each map took approximately 3 hours to form. Black contours are streamlines of the rotational component of the high-pass surface velocity field (see Methods). Shading shows the vorticity (left panels) and divergence (right panels) normalized by the Coriolis frequency, f, corresponding to a period of about 20 hours.

2 Submesoscale eddies between two mesoscale eddies

The domain mapped by DopplerScatt between October 24 and 26 (black rectangle in Extended Data Fig.1c) is located between a cold cyclonic eddy centered at 37°N, 124.5°W ('C' in Extended Data Fig.1c) and a warm anticyclonic eddy at 36°N, 126°W ('A' in Extended Data Fig.1c). Both mesoscale eddies have a size of ∼150 km and horizontal geostrophic velocities of ∼0.3 to 0.4 m s^{-1}. These mesoscale eddies were identified from satellite altimetry and remained nearly stationary during the three days. A cloud-free sea surface temperature (SST) satellite image was available only on the last day (Extended Data Fig. 1c,d), displaying a roughly zonal SST front between the two mesoscale eddies with a temperature gradient reaching 0.5 °C km^{-1} (Extended Data Fig.1d). Each day, DopplerScatt observations revealed the presence of about 20 submesoscale eddies in the 30 km × 100 km domain, with their sizes

ranging from 2 km up to 20 km (Fig. 1b). These eddies are found on both sides of a eastward zonal flow roughly located around a latitude of 36.8°N. The SST satellite image on October 26 suggests this zonal flow is related to the SST front. Fig. 1b emphasizes that the submesoscale eddies evolve from one day to the other and even within 6 hours (Fig. 2).

Dynamics of the submesoscale eddies are also reflected in the statistics of their associated velocity gradients, such as vorticity, strain, and divergence (see Methods), which were calculated after smoothing the DopplerScatt velocities using a Gaussian spatial filter with a full-width half maximum of 2 km (Fig. 3). Vorticity, strain and divergence at this scale have an RMS value of order f. The vorticity reaches a maximum close to $4f$, whereas negative values have a much smaller magnitude. This skewness (1.27 here) has been observed previously in some ship-based surveys [3, 14, 15]. Divergence is slightly negatively skewed, with an RMS value somewhat less than vorticity. Assuming the divergence is uniform in the upper half of the mixed-layer leads to vertical velocities with maxima of 250 m day^{-1} at a depth of 40 m and an RMS value of 75 m day^{-1}, a value two times larger than estimated in numerical models with a spatial resolution of 500 m[16].

Extended Data Figs. 2, 3,-4 further reveal that the submesoscale patterns of vorticity, strain, and divergence exhibit conspicuous dipole structures in between eddies over three consecutive days (white lines in Extended Data Figs. 2, 3,-4), with the vorticity patterns anticorrelated with divergence patterns (see also Extended Data Fig.7a). This suggests that the divergence field, and therefore the vertical velocity field associated with submesoscale eddies, is principally driven by the interactions between cyclonic and anticyclonic eddies.

The DopplerScatt velocities show kinetic energy distributed over a wide range of scales (Fig. 3c), as characteristic of strongly nonlinear turbulent flows. The kinetic-energy spectrum approximately follows a power law k^{-2} between 2 to 40 km with k the wavenumber, which is consistent with numerical studies [17–21] and in situ observations [22] of energetic submesoscale turbulence. Furthermore, a power law k^{-2} indicates that while smaller-scale eddies have less kinetic energy than larger-scale eddies, velocity gradients are dominated by the submesoscale eddies [23]. Roughly, the RMS values of divergence and vorticity at 2 km are ten times as large as they are at 200 km (see Methods and Fig. 3d), indicating a shift in dynamics between mesoscale and submesoscale eddies.

3 The dynamical balance of submesoscale eddies diverge from the mesoscale

The strong curvature and large velocity gradients associated with submesoscale eddies (Fig. 1b) suggest these eddies may be affected by centripetal forces and therefore are not in geostrophic balance. Geostrophic balance occurs when the Coriolis forces,

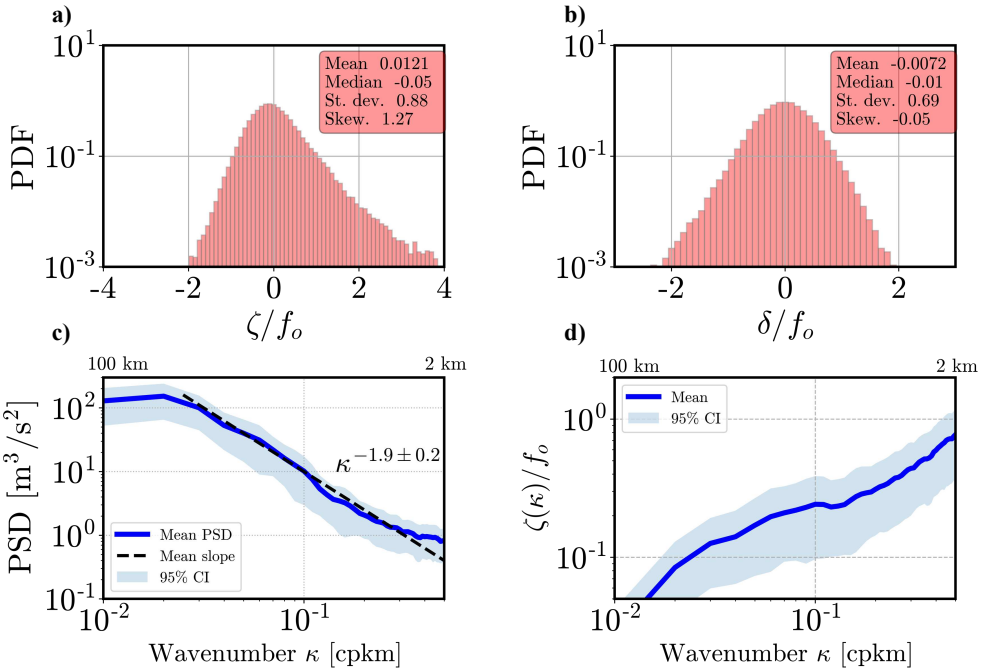


Fig. 3: **Statistics of submesoscale motions**. Probability density histograms of surface relative vorticity (a), divergence (b) normalized by the Coriolis frequency f_o. Velocity gradients were computed from DopplerScatt observations smoothed to 2 km. (c) Power spectral density for unfiltered DopplerScatt surface currents. The mean spectral slope between in the 2-40 km wavelength range is in $\kappa^{-1.9\pm0.2}$ computed from least-square fitting. (d) Spectrum of vorticity normalized by f_o. The shaded region represents the 95% confidence interval from the mean spectrum based on the spread of spectral realizations across flights.

$f\boldsymbol{z}\times\boldsymbol{u}$, almost balance the pressure gradients, $\nabla p/\rho$, in the momentum equation,

$$\frac{\mathrm{d}\boldsymbol{u}}{\mathrm{d}t} + f\boldsymbol{z}\times\boldsymbol{u} = -\frac{\nabla p}{\rho}, \tag{1}$$

where $\boldsymbol{u}$ is the velocity, $\boldsymbol{z}$ is a unit vector pointing up, p is pressure, and ρ is density. Indeed, such strong curvature usually supplies an additional inward centripetal force, included in the acceleration of fluid parcels, $\mathrm{d}\boldsymbol{u}/\mathrm{d}t$, causing eddies to evolve much faster than mesoscale eddies, which are associated with weaker curvature [24].

We quantify the departure of submesoscale eddies from geostrophic balance through the analysis of the horizontal divergence of the momentum equation (1) (see Methods). Maps of the divergence of the accelerations (Fig. 4a) and of the divergence of the Coriolis term (Fig. 4b) indicate that both contributions have similar magnitudes. The divergence of the accelerations is largest between eddies, which emphasizes the

impact of Lagrangian accelerations on eddy interactions as found in numerical studies [25, 26]. A substantial departure from geostrophic balance occurs, as expected, where the Rossby number is large (Fig. 4d). In addition, when the explicit contribution of the divergence (δ) is not taken into account in Eq.6 (see Methods), the departure from geostrophy is weaker: the differences between Fig.4d and e highlight the impact of δ in the momentum balance of submesoscale eddies.

Lagrangian accelerations, $\mathrm{d}\boldsymbol{u}/\mathrm{d}t$, also impact the dispersion of particles and tracers, leading them to move around eddies and ultimately fill the whole eddy field [27, 28]. The key quantities involved in the dispersion mechanisms are the strain, σ, relative vorticity, ζ, and divergence, δ (see Methods). We have estimated the dispersion of particles and tracers embedded in the submesoscale eddy field using the Okubo-Weiss quantity[28] (involving the strain and vorticity fields) diagnosed from DopplerScatt observations (see Eqs. 8 and 9 in Methods, and Extended data Figure 5). The separation distance between two particles increases from 1 km to 50 km in just 12 hours. The same increase takes more than 20 days if only the mesoscale eddy field observed by altimeter products is present. This highlights the strong efficiency of submesoscale eddies to quickly disperse any tracers and particles.

These results indicate that the large magnitude of the Lagrangian accelerations associated with the strong curvature of submesoscale eddies explains the fast interactions between these eddies within a few hours, compared with the slow time evolution of mesoscale eddies. They further emphasize the strong relationship between submesoscale eddy interactions and divergence.

4 Submesoscale interactions and divergence

Eddy interactions are usually assessed through KE transfer between scales. We have estimated the cross-scale KE transfer associated with submesoscales using a coarse-graining approach that estimates the KE transfer between large (>5 km) and small (<5 km) scales [29, 30] (Methods). Similar results are obtained if the threshold is set to larger (7 km) or smaller scales (3 km) than 5 km. The cross-scale KE transfer magnitude is largest in between submesoscale eddies (Fig. 5a). These transfers can be either positive or negative, with their magnitudes of the order of 2×10^{-7} m^2 s^{-3}, which corresponds to a KE change of about 0.004 m s^{-1} within 6 hours. The KE of scales smaller than 5 km has a magnitude of up to 0.01 m^2 s^{-2} and is located in the same regions as the KE transfers, i.e., in-between submesoscale eddies (Fig. 5b). This indicates that the KE at small scales can increase or decrease by a factor of about two at the expense or benefit of larger scales within a few hours. These observational results are remarkably similar to those from a recent numerical study by Srinivasan et al. [30] in the Northeast Atlantic, not only in terms of the location of KE at small scales and KE transfer with respect to submesoscale eddies but also in terms of the order of magnitude of these quantities.

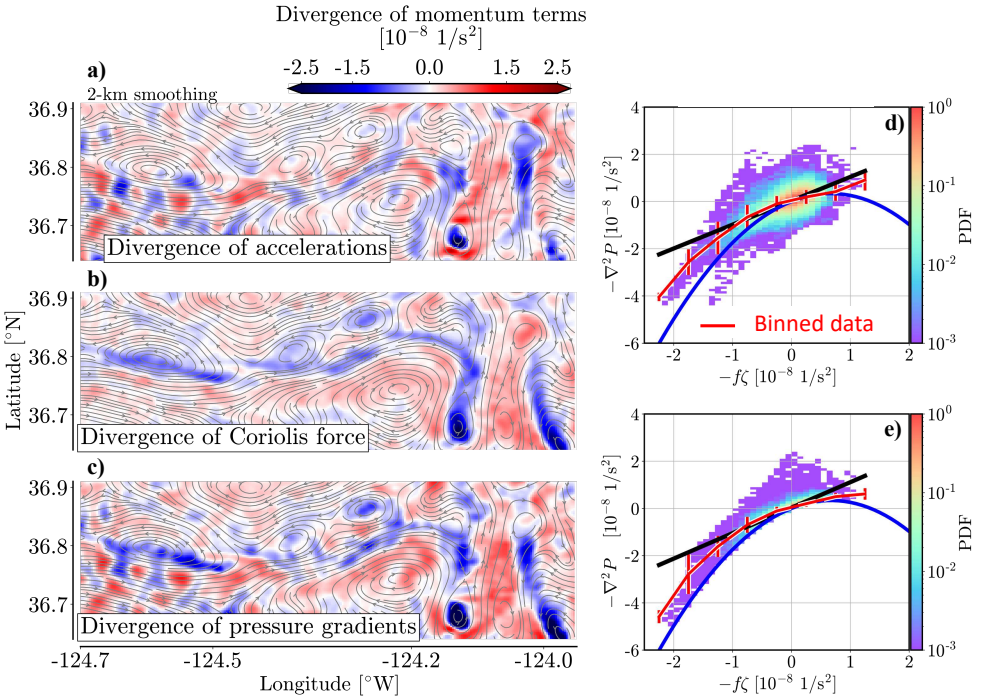


Fig. 4: **Dynamical balance**: (a) Divergence of accelerations, (b) divergence of Coriolis forces, and (c) divergence of pressure gradients estimated from the divergence budget (Eq. 6) (see Methods). The maps in (a)-(c) corresponds to October 26^{th}, 2022 at 21:44 UTC. (d) Scatterplot between the divergence of pressure gradients and divergence of Coriolis forces. The solid black line represents a balance between the divergence of pressure gradients and divergence of Coriolis forces, or geostrophic balance. (e) The same as panel (d) except that the pressure Laplacian is estimated from Eq. 6 without considering δ. The blue curve is an approximation of the ageostrophic balance ($-\nabla^2 P_{ag} = -\frac{\zeta^2}{2} + f\zeta$). Four consecutive DopplerScatt flights (from October 24 to October 26) were used to construct the scatterplots. The uncertainty in the estimation of the divergence of pressure gradients is smaller than 10% of f^2 at 2-km scale (see SI).

Scale transfers of KE are governed by the strain and divergence of larger scales (see Eq. 12 in Methods and Extended Data Fig. 7). For divergent flows, KE transfers can go to either small or large scales, whereas purely rotational flows tend only to transfer energy to larger scales[31, 32]. Here, we analyze the specific contribution of the divergence to these KE transfers. DopplerScatt measurements from four consecutive flights reveal that in-between submesoscale eddies, there is a dipole of divergence anticorrelated with KE transfer (white lines in Extended Data Figs. 3, 6). On average, KE transfers have the opposite sign as divergence (Fig. 5c, see also Extended Data Fig. 7), emphasizing the relationship between divergence and submesoscale

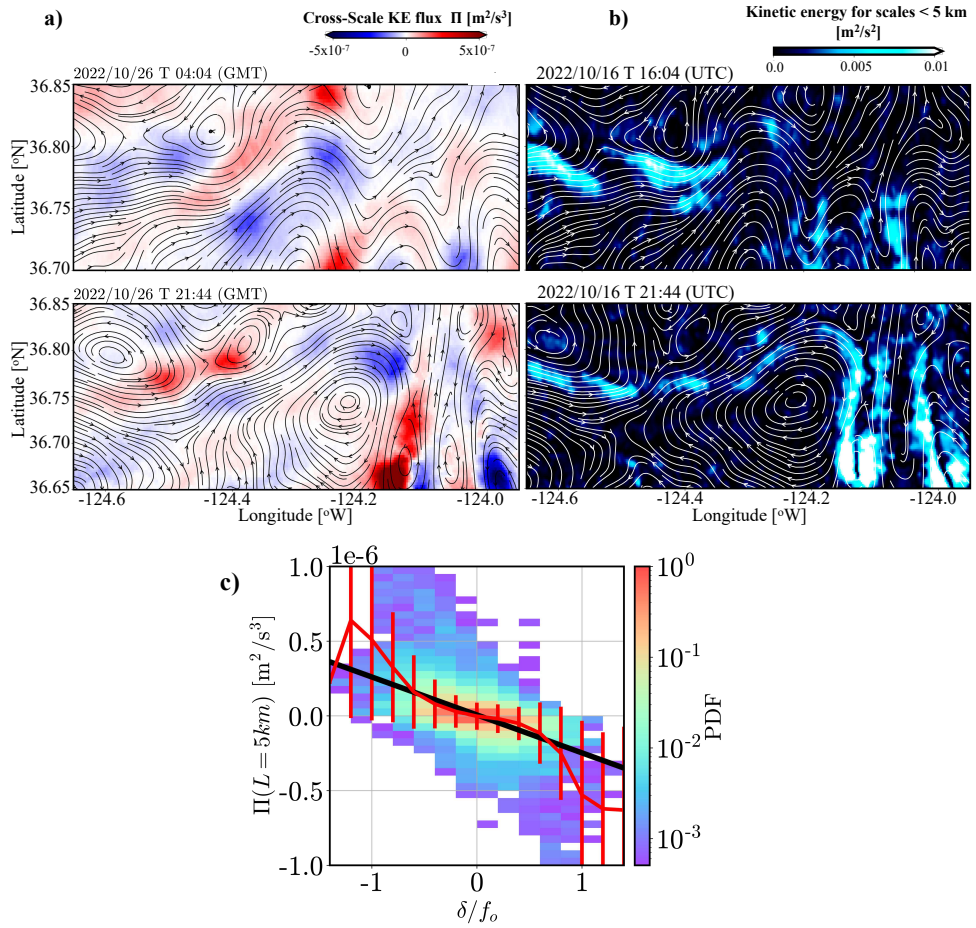


Fig. 5: **Cross-scale submesoscale interactions.** (a) Surface cross-scale kinetic energy flux (Π) through 5 km scales, computed with a coarse-graining approach: Red (blue) color represents kinetic energy flux from larger (smaller) scales to smaller (larger) scales relative to 5 km. (b) Surface kinetic energy for scales smaller than 5 km. (c) Relationship between divergence (δ) and cross-scale kinetic energy flux (Π) using the four flights.

interactions. The four flights are not enough to conclude whether submesoscale eddies contribute to the net transfer energy to large scales, leading to strengthened mesoscale eddies, or to small scales, leading to KE dissipation. The KE transfers from four flights produce an average transfer $6.0 \pm 2.2 \times 10^{-9}$ m^2 s^{-3} (95 % CI, 480 DOF) to small scales, indistinguishable from zero. More flights are needed to accumulate sufficient statistics for a robust estimate of the net transfer.

5 Summary and Discussion

DopplerScatt measurements reveal a large number of interconnected submesoscale eddies evolving over a period of a few hours. These observations provide direct evidence that cross-scale interactions, over a scale range from 1 km down to 100 km, lead to large horizontal divergence at submesoscales and vertical velocities reaching 250 m day^{-1} at a depth of 40 m. These results emphasize that cross-scale interactions may profoundly affect the vertical transport of heat, carbon, and important climatic gases, as well as the horizontal dispersion of tracers and particles, which emphasizes the need to consider these unresolved interactions in climate models.

The DopplerScat velocity fields highlight the existence of many dipole structures in between eddies that characterize their interactions. The anticorrelation between vorticity and divergence within these dipoles is suggestive of the relationships predicted by frontogenesis theory [33]: cyclonic vorticity tends to be associated with surface convergence ($\delta < 0$) and thus downwelling (usually found in the cold side of a front), whereas anticyclonic vorticity tends to be associated with divergence ($\delta > 0$) and thus upwelling (warm side of a front).

Important questions remain related to the interactions between mesoscales and submesoscales: (i) what instabilities (shear instability, convective instability, frontal or mixed-layer instabilities) energize submesoscale eddies and (ii) what is the net direction and strength of the KE transfer between scales over larger scales. Addressing these questions would require observations of submesoscale turbulence over a domain large enough to capture a full mesoscale/submesoscale eddy field, such as a 200 km $\times$ 200 km domain, as well as persistent access to high-resolution SST images.

We have compared our results with those from a numerical model with a spacing grid resolution of 500 m, configured for the CCS region during the same season as the S-Mode experiment. Statistics for the vorticity, divergence and Okubo-Weiss quantity from numerical outputs, spatially smoothed to 2-km as the DopplerScatt observations, reveal RMS values that are 2.5 times smaller than those diagnosed from observations (Extended Data Fig. 9). Furthermore, the modeled submesoscale structures exhibit principally elongated patterns that differ from the dipole structures revealed by DopplerScatt observations. These differences question the pertinence of existing numerical models to fully reproduce submesoscale dynamics and, in particular, what mechanisms need to be included in these models.

6 Methods

6.1 Sub-Mesoscale Ocean Dynamics Experiment (S-MODE)

The S-MODE project is a NASA Earth Ventures Suborbital Investigation designated to test the hypothesis that kilometer-scale ocean eddies make important contributions to the vertical exchange of climate and biological variables in the upper ocean[13]. A full description of the S-MODE project can be found in S-MODE. The most novel aspect of S-MODE is the deployment of airborne instruments, in particular the DopplerScatt instrument whose observations collected in October 2022 are the scope of this study.

6.2 Satellite altimetry and geostrophic approximation

The background mesoscale eddy field present in the S-Mode domain (126.5-122°W, 35.5-39°N) has been inferred from the sea surface height (SSH) provided by the Near-Real-Time gridded SSALTO/DUACS SSH L4 product http://marine.copernicus.eu. Based on Ballarta et al.[34], the effective spatial resolution of the gridded anomalies is approximately 150 km in wavelength. SSH is composed of the mean dynamic topography [35] and the sea level anomaly maps produced by the DUACS (data unification and altimeter combination system) processing that merges the multi-altimeter along-track constellation. Mesoscale velocities have been diagnosed from SSH using the geostrophic approximation, as follows:

$$\boldsymbol{z} \times \boldsymbol{u} = -\frac{g}{f} \cdot \nabla SSH, \tag{2}$$

with $\boldsymbol{z}$ the vertical unit vector, $\boldsymbol{u}$ the velocity vector, f the Coriolis frequency and g the gravitational constant.

6.3 Satellite Infrared Image

The Sea Surface Temperature (SST) has been estimated from satellite infrared images provided by Group for High Resolution Sea Surface Temperature (GHRSST) and the National Oceanic and Atmospheric Administration (NOAA) http://www.ghrsst.org. L2P SST fields were used, as measured by Visible Infrared Imaging Radiometer Suite (VIIRS) instrument, at a spatial resolution of 0.0067°. For a quick access to SST collection covering S-MODE experiments, a catalog of satellite SST images are stored in the following link http://smode.whoi.edu/satellite/.

6.4 Surface velocities from NASA-JPL DopplerScatt observations

This paper focuses on novel airborne ocean surface velocities carried out by the NASA-JPL Doppler Scatterometer (DopplerScatt) instrument[12, 36, 37], flying on a NASA King Air B200 aircraft.

DopplerScatt is a radar operating at Ka-band. It provides simultaneous measurements of 10-m height ocean surface equivalent neutral winds and vector surface currents tuned to a 4 m depth. The Ka-band signal propagates through clouds, making the system unconstrained by clear weather requirements. However, this is not the case during rain events where DopplerScatt signal could be contaminated. DopplerScatt operated only during free-rain conditions during S-MODE in October 2022.

DopplerScatt is capable of mapping out two-dimensional swaths in latitude-longitude with dimensions of 100 km along-track and 25 km across-track, at a cruise velocity of 250 knots and an altitude of 28,000 feet. The single swaths were covered in $\sim$ 15 minutes. A total of 12 single-swaths were performed per flight, with an overlapping of 70%. This allows the coverage of the area sketched in Fig.6d,e in 3 hours. It is worth noting that 15 minutes per single-swath permit to capture the fast evolving nature of the submesoscale eddies reported in this study (see Fig.2SI). Finally, the ground processing of multiple passes allow to reduce the random errors by leveraging the partial overlapping of the footprint. The pixel resolution achieved is 200 m with a random noise level $< O(0.04\ \mathrm{m\,s^{-1}})$. The principles of measurement and validation of DopplerScatt were described in the context of a field campaign in the Gulf of Mexico [12, 36, 37].

An estimation of the error of diagnosed velocity gradients has been done (see SI part). The velocity gradients were calculated using a centered difference scheme. The error associated to the velocity gradients computed using the unsmoothed velocities can be as large as f_o, with $f_o = 0.8 \times 10^{-4}\ \mathrm{s^{-1}}$. However, a Gaussian spatial filter were used to reduce the noise in the velocity gradients, with an e-folding scale L_G ($L_G = (L/2.3548)/pixel_{size}$, where L is the spatial averaging scale associate to the full width half maximum of the Gaussian smoother, and $pixel_{size} = 200$ m) (see SI). Using a Gaussian filter with a full width half maximum of 2 km, the error reaches $0.15 f_o$ at the center of the domain and $0.3 f_o$ at the edges of the domain (see SI).

6.5 Frontal tendency

Continuing the rationale of comparing the properties between mesoscale and submesoscale eddies, the time scale of the stretching of the SST front by the two eddy fields is given by the frontal tendency estimated as [16]:

$$\frac{1}{|\nabla_h T|^2}\frac{d}{dt}(|\nabla_h T|^2) = -\frac{1}{2|\nabla_h T|^2}[S_n(T_x^2 - T_y^2) + S_s.T_x.T_y]\ . \tag{3}$$

t is the time. $d(.)/dt$ is the Lagrangian time derivative: $d(.)/dt = \partial(.)/\partial t + \mathbf{U}.\nabla(.)$. T is the SST, and $|\nabla_h T|^2 = T_x^2 + T_y^2$. S_n and S_s are the normal and shear strains as $S_n = 2U_x$, $S_s = U_y + V_x$ with, U,V given by the low-pass ($>$ 15 km) and high-pass ($<$ 15 km) DopplerScatt velocity. On the one hand, the low-pass strain field is related to the mesoscale eddy field. On the other hand, the high-pass strain field is related to the submesoscale eddy field. The frontal tendency associated to high-pass velocity is shown in Fig.1c and the frontal tendency associated to the mesoscale field is shown

in Extended Data Fig.1. Both Frontogenetic fields can be related to a time to a time scale [33]. Over the SST front, the low-pass frontal tendency is $\sim 5.10^{-6}\mathrm{s}^{-1}$, corresponding to a time scale of $\sim$ two days. Whereas the high-pass frontal tendency is $\sim 5.10^{-5}\mathrm{s}^{-1}$, corresponding to a time scale of $\sim$ 5 hours.

6.6 Velocity power spectral density

A multitaper spectral analysis was performed on a 100 km slices along DopplerScatt flight tracks to estimate power spectral density of ocean surface currents. About 200 independent spectral realizations per flight were averaged together to reduce noise. DopplerScatt currents were interpolated onto a regular grid using a cubic spline interpolation with a spacing of 200 m. The spectral slope and its standard error was estimated using least-square fitting.

DopplerScatt velocities are characterized by a KE spectral slope close to k^{-2} between 2 km to 40 km with k the wavenumber (Fig. 3d). From these spectral characteristics, smaller eddies have smaller KE than larger eddies but larger velocity gradients. Indeed, velocity gradient magnitudes can be expressed in terms of k[23, 38] as $[k^3 KE(k)]^{1/2}$, with $KE(k)$ the power spectral density of KE at wavenumber k with units of $\mathrm{m}^3\ s^{-2}$. Thus, for a k^{-2} spectrum slope, velocity gradients are proportional to $k^{2/3}$. This means that an eddy with a size of 2 km will have velocity gradients about 10 times larger than those for an eddy with a size of 200 km (Fig. 4d). Since large velocity gradients are expected at small scales, KE at small scales should be found where large velocity gradients are located, i.e. in-between submesoscale eddies. The implications of this result are discussed below.

6.7 Diagnosing Lagrangian accelerations

The time evolution of surface velocities is driven by pressure forces through the momentum equations:

$$\frac{d\boldsymbol{u}}{dt} + f \cdot \boldsymbol{z} \times \boldsymbol{u} = -\nabla P, \tag{4}$$

with P the pressure. The geostrophic balance implies that pressure gradients are balanced by the Coriolis forces, i.e.

$$f.\boldsymbol{z} \times \boldsymbol{u} \approx -\nabla P, \tag{5}$$

and therefore that the acceleration terms, $\frac{d\boldsymbol{u}}{dt}$ are much smaller than the Coriolis forces.

To infer the dynamical balance of submesoscale eddies, we have considered the divergence of the momentum equations:

$$\overbrace{\frac{\partial \delta}{\partial t} + \boldsymbol{u}.\nabla\delta + \frac{\sigma^2 - \zeta^2}{2} + \frac{\delta^2}{2}}^{ageostrophic\ balance} \underbrace{-f\zeta = -\nabla^2 P}_{geostrophic\ balance} . \tag{6}$$

The first four terms in Eq.6 ($\partial\delta/\partial t + \boldsymbol{u}.\nabla\delta + \delta^2/2 + (\sigma^2 - \zeta^2)/2$) correspond to the divergence of the Lagrangian accelerations, the fifth term ($-f\zeta$) to the divergence of the Coriolis forces, and the last term to the divergence of pressure gradients ($-\nabla^2 P$). When the divergence of the Lagrangian accelerations has a magnitude similar to the divergence of the Coriolis forces, the dynamical balance is not geostrophic. It is called a ageostrophic balance[23, 39].

Terms in Eq. 6 have been computed from DopplerScatt velocities except for the last term which is treated as a residual term. The first term, the divergence tendency, is estimated from the change in divergence between the two panels of 2a. DopplerScatt observations indicate that the Eulerian time derivative of the divergence, the first term in Eq.6, is smaller than the other terms on the left-hand side. The smallness of the divergence tendency, $\partial\delta/\partial t$, compared with the nonlinear terms, in particular, the third and fourth terms in Eq. 6, strongly suggests that internal gravity waves, usually explained by linear dynamics[38], have a very weak impact on the velocity field analyzed in this study.

We have assessed the accuracy of closing the budget in eq.6 by testing the budget vorticity equation using the two DopplerScatt flights on October 26.

$$\frac{\partial \zeta}{\partial t} + u \cdot \nabla\zeta + (f + \zeta) \cdot \delta = 0 \tag{7}$$

The budget is nonzero, but note that the budget were computed using the two flights separated by 6 hours. Closing the budget is challenging since submesoscale evolved in less than 6 hours. In order to estimate an error in the vorticity budget equation, the stretching term was used as reference to define relative error. Fig.12SI shows the relative error of smoothed vorticity budget equation. The relative error as a function of spatial smoothing revealed that the smallest relative error is between 2 km and 5 km. And the error accounts for 10% f_o^2.

6.8 Eddy interactions driven by strain, vorticity, divergence, Okubo-Weiss quantity. Dispersion of particles

One approach to diagnosing the dynamical properties of a turbulent flow in terms of eddy interactions is to analyze the dispersion of particles [26]. If $\delta\mathbf{X}$ is the separation

distance between two particles, its time evolution is given by [27]:

$$\frac{d}{dt}\delta\mathbf{X} = \frac{1}{2}\begin{bmatrix}\delta+\sigma_n & \sigma_s-\zeta\\ \sigma_s+\zeta & \delta-\sigma_n\end{bmatrix}\delta\mathbf{X}\,, \tag{8}$$

where σ_n and σ_s are respectively the normal and shear strains defined as $\sigma_n = u_x - v_y$ and $\sigma_s = v_x + u_y$. ζ is the vorticity defined as $\zeta = v_x - u_y$ and $\delta = u_x + v_y$ is the divergence. The total strain is $\sigma = \sqrt{\sigma_n^2 + \sigma_s^2}$. Then, a solution of eq.8 is:

$$\delta\mathbf{X}(t) \approx \delta\mathbf{X}(0).e^{t.(\delta \pm Q^{1/2})/2}, \tag{9}$$

with Q the Okubo-Weiss quantity defined as:

$$Q = \sigma^2 - \zeta^2. \tag{10}$$

Q quantifies the competition between strain and vorticity. When $Q > 0$, Eq.9 indicates an exponential growth or decay of $\delta\mathbf{X}$ since strain dominates: particles diverge, or are dispersed in one direction and converge in the other direction. When $Q < 0$ is negative, vorticity dominates and therefore there is no growth or decay of $\delta\mathbf{X}$, just a rotation the particles since $Q^{1/2}$ is purely imaginary. Eq.9 also emphasizes the direct contribution of the divergence. Thus, if the divergence is negative, particles converge.

From DopplerScatt observations, the RMS values of Q and δ are respectively f^2 and $0.69f$. Using $|Q|^{-1/2} \approx f^{-1}$ (with $f = 0.8 \times 10^{-4}\mathrm{s}^{-1}$), this leads to a time scale of about three hours. From eq.9, we can infer the particle dispersion due to the submesoscale turbulent field: the separation distance between two particles, roughly given by $\delta\mathbf{X}(t) \approx \delta\mathbf{X}(0).\exp\left[\pm Q^{1/2}.t\right]$ [28], increases from 1 km up to 50 km in 12 hours. The same increase will take more than 20 days if only the mesoscale eddy field is present (for which $|Q|^{1/2} < 0.05f$), which highlights the strong impact of submesoscale turbulence on the 2-D dispersion.

6.9 Kinetic energy fluxes across scales

The scale kinetic energy flux ($\Pi(L)$) is the rate of transfer of kinetic energy between scales smaller than a specific horizontal scale L and scales larger than L [30]. The coarse-graining approach is used to estimate the fluxes [29]. This method has been widely used to investigate kinetic energy fluxes between mesoscale eddies and scales between 1-50 km [30].

The method relies on a low-pass filter through a convolution $\overline{F}(x,y) = C \times F(x,y)$ with a top-hat kernel

$$C(\mathbf{r}) = \begin{cases}1/A, & \text{if } |\mathbf{r}| < L/2.\\ 0, & \text{otherwise.}\end{cases} \tag{11}$$

where $A = \pi L^2/4$ is the circular normalization area of diameter L and $\mathbf{r}$ is the radial position vector.

We employed the same filter here as in the literature to be able to compare the magnitude of the fluxes. These fluxes are given by (see refs[29, 30] for the derivation):

$$\Pi(\mathbf{L}) = \left(\overline{u'^2} - \overline{v'^2}\right)\frac{\overline{\sigma_n}}{2} - \overline{u'v'}\,\overline{\sigma_s} - \left(\overline{u'^2} + \overline{v'^2}\right)\frac{\overline{\delta}}{2}, \tag{12}$$

where prime (overline) velocities are obtained using a high-pass (low-pass) filter using L as a threshold. The computation of Π was performed in a regular grid with 200 m grid spacing using DopplerScatt velocities without previous smoothing to avoid confusion. We have chosen $L = 5$ km.

Negative values of Π are associated with upscale kinetic energy flux (from smaller scales to larger scales relative to L) and positive values with downscale (from larger scales to smaller scales relative to L). Estimation of Π using DopplerScatt data revealed that the terms related to strain, σ_n and σ_s, have the same order of magnitude as the term related to divergence, δ. The term related to divergence emphasizes that the time scale associated with kinetic energy ($\overline{u'^2} + \overline{v'^2}$), is the divergence time scale, i.e. a few hours. This is consistent with the fast time evolution of the submesoscale eddy field.

6.10 High-resolution regional ocean numerical simulation

A numerical ocean simulation was performed in the California Current System. The heart of the simulation is the Massachusetts Institute of Technology General Ocean Circulation (MITgcm) architecture. The domain covers the S-MODE region and it was integrated from December 1st, 2011, to November 1st, 2012. The spacing grid resolution is 500 m and has 90 vertical levels [16].

Acknowledgements

This work was performed at the Jet Propulsion Laboratory, California Institute of Technology under prime contract with NASA (80NM0018D0004), and was awarded under NASA Research Announcement (NRA) NNH17ZDA001N-EVS3, Research Opportunities in Space and Earth Science (ROSES-2017), Appendix A.34: Earth Venture Suborbital-3; NASA Sub-Mesoscale Ocean Dynamics Experiment (NASA S-MODE). Copyright 2024 California Institute of Technology. US government sponsorship acknowledged. PK acknowledges support from the SWOT Science Team, the NASA S-MODE project and the QuickSCat mission. This study has been much inspired and motivated by the S-MODE project and the DopplerScatt instrument. The DopplerScatt team extends its gratitude to the crew of pilots and ground crew of the NASA King Air B200 aircraft for all the support during S-MODE field campaigns.

©2024 California Institute of Technology. Government sponsorship acknowledged.

Declarations

- **Authors' contributions** H.T. and P.K. led the data analysis and data interpretation. H.T, P.K., E.R., A.W., E.D., A.T., J.C. drafted the manuscript. E.R. and A.W. processed DopplerScatt. T.F., E.D., and E.R. led the S-MODE experiment. D.P.-M. led DopplerScatt instrument. H.T., A.W., F.P. and R.K. were DopplerScatt operators during S-MODE experiment. All authors contributed to the scientific interpretation of the results and reviewed the manuscript.

- **Funding** This research was carried out at the Jet Propulsion Laboratory, California Institute of Technology, under a contract with the National Aeronautics and Space Administration (NASA).

- **Conflict of interest/Competing interests** The authors declare no competing interests.

- **Ethics approval** Not applicable
- **Consent to participate** Not applicable
- **Consent for publication** Not applicable
- **Availability of data and materials** Data of DopplerScatt for the S-MODE experiment can be download through PO.DAAC data portal: DopplerScatt dataset. A closer look of the data used in this manuscript can be found at: S-MODE-closer-look.
- **Code availability** Code and examples, along with video explanations for working with DopplerScatt data are available from PO.DAAC's GitHub page, S-MODE GitHub.

If any of the sections are not relevant to your manuscript, please include the heading and write 'Not applicable' for that section.

Editorial Policies for:

Springer journals and proceedings: https://www.springer.com/gp/editorial-policies

Nature Portfolio journals: https://www.nature.com/nature-research/editorial-policies

Scientific Reports: https://www.nature.com/srep/journal-policies/editorial-policies

BMC journals: https://www.biomedcentral.com/getpublished/editorial-policies

References

[1] Munk, W., Armi, L., Fischer, K. & Zachariasen, F. Spirals on the sea. *Proceedings of the Royal Society of London. Series A: Mathematical, Physical and Engineering Sciences* **456**, 1217–1280 (2000).

[2] Ni, Q., Zhai, X., Wilson, C., Chen, C. & Chen, D. Submesoscale eddies in the south china sea. *Geophysical Research Letters* **48**, e2020GL091555 (2021).

[3] Shcherbina, A. Y. *et al.* Statistics of vertical vorticity, divergence, and strain in a developed submesoscale turbulence field. *Geophysical Research Letters* **40**, 4706–4711 (2013).

[4] Poje, A. C. *et al.* Submesoscale dispersion in the vicinity of the deepwater horizon spill. *Proceedings of the National Academy of Sciences* **111**, 12693–12698 (2014).

[5] Thompson, A. F. *et al.* Open-ocean submesoscale motions: A full seasonal cycle of mixed layer instabilities from gliders. *Journal of Physical Oceanography* **46**, 1285–1307 (2016).

[6] D'Asaro, E. A. *et al.* Ocean convergence and the dispersion of flotsam. *Proceedings of the National Academy of Sciences* **115**, 1162–1167 (2018).

[7] Yu, X. *et al.* An annual cycle of submesoscale vertical flow and restratification in the upper ocean. *Journal of Physical Oceanography* **49**, 1439–1461 (2019).

[8] Siegelman, L. *et al.* Enhanced upward heat transport at deep submesoscale ocean fronts. *Nature Geoscience* **13**, 50–55 (2020).

[9] Balwada, D., Xie, J.-H., Marino, R. & Feraco, F. Direct observational evidence of an oceanic dual kinetic energy cascade and its seasonality. *Science Advances* **8**, eabq2566 (2022).

[10] Taylor, J. R. & Thompson, A. F. Submesoscale dynamics in the upper ocean. *Annual Review of Fluid Mechanics* **55**, 103–127 (2023). URL https://www.annualreviews.org/content/journals/10.1146/annurev-fluid-031422-095147.

[11] Alexakis, A. *et al.* Large-scale self-organization in dry turbulent atmospheres. *Science* **383**, 1005–1009 (2024).

[12] Rodriguez, E. On the optimal design of doppler scatterometers. *Remote Sensing* **10** (2018). URL https://www.mdpi.com/2072-4292/10/11/1765.

[13] Farrar, J. T. *et al. S-mode: The sub-mesoscale ocean dynamics experiment*, 3533–3536 (IEEE, 2020).

[14] Rudnick, D. L. On the skewness of vorticity in the upper ocean. *Geophysical Research Letters* **28**, 2045–2048 (2001). URL https://onlinelibrary.wiley.com/doi/abs/10.1029/2000GL012265.

[15] Buckingham, C. E. *et al.* Seasonality of submesoscale flows in the ocean surface boundary layer. *Geophysical Research Letters* **43**, 2118–2126 (2016).

[16] Torres, H. S. *et al.* Separating energetic internal gravity waves and small-scale frontal dynamics. *Geophysical Research Letters* **49**, e2021GL096249 (2022).

[17] Fox-Kemper, B., Ferrari, R. & Hallberg, R. Parameterization of mixed layer eddies. part i: Theory and diagnosis. *Journal of Physical Oceanography* **38**, 1145–1165 (2008).

[18] Callies, J., Ferrari, R. & Bühler, O. Transition from geostrophic turbulence to inertia–gravity waves in the atmospheric energy spectrum. *Proceedings of the National Academy of Sciences* **111**, 17033–17038 (2014).

[19] Capet, X., McWilliams, J. C., Molemaker, M. J. & Shchepetkin, A. F. Mesoscale to submesoscale transition in the California Current System. part i: Flow structure, eddy flux, and observational tests. *Journal of physical oceanography* **38**, 29–43 (2008).

[20] Klein, P. High-frequency winds and eddy-resolving models. *Ocean Modeling in an eddying regime. AGU Monograph Series. AGU* 83–100 (2008).

[21] McWilliams, J. C. Submesoscale currents in the ocean. *Proc. R. Soc. A* **472**, 20160117 (2016).

[22] Callies, J., Ferrari, R., Klymak, J. M. & Gula, J. Seasonality in submesoscale turbulence. *Nature communications* **6**, 1–8 (2015).

[23] Capet, X., McWilliams, J. C., Molemaker, M. J. & Shchepetkin, A. F. Mesoscale to submesoscale transition in the california current system. part iii: Energy balance and flux. *Journal of Physical Oceanography* **38**, 2256–2269 (2008).

[24] Shakespeare, C. J. Curved density fronts: Cyclogeostrophic adjustment and frontogenesis. *Journal of Physical Oceanography* **46**, 3193–3207 (2016).

[25] Hua, B. L. Skewness of the generalized centrifugal force divergence for a joint normal distribution of strain and vorticity components. *Physics of Fluids* **6**, 3200–3202 (1994).

[26] Hua, B. L., McWilliams, J. C. & Klein, P. Lagrangian accelerations in geostrophic turbulence. *Journal of Fluid Mechanics* **366**, 87–108 (1998).

[27] Okubo, A. *Horizontal dispersion of floatable particles in the vicinity of velocity singularities such as convergences*, Vol. 17, 445–454 (Elsevier, 1970).

[28] Weiss, J. The dynamics of enstrophy transfer in two-dimensional hydrodynamics. *Physica D: Nonlinear Phenomena* **48**, 273–294 (1991).

[29] Aluie, H., Hecht, M. & Vallis, G. K. Mapping the energy cascade in the north atlantic ocean: The coarse-graining approach. *Journal of Physical Oceanography* **48**, 225–244 (2018).

[30] Srinivasan, K., Barkan, R. & McWilliams, J. C. A forward energy flux at submesoscales driven by frontogenesis. *Journal of Physical Oceanography* **53**, 287–305 (2023).

[31] Marino, R., Mininni, P. D., Rosenberg, D. & Pouquet, A. Inverse cascades in rotating stratified turbulence: fast growth of large scales. *Europhysics letters* **102**, 44006 (2013).

[32] Pouquet, A., Marino, R., Mininni, P. D. & Rosenberg, D. Dual constant-flux energy cascades to both large scales and small scales. *Physics of Fluids* **29** (2017).

[33] Hoskins, B. J. & Bretherton, F. P. Atmospheric frontogenesis models: Mathematical formulation and solution. *Journal of the Atmospheric Sciences* **29**, 11–27 (1972).

[34] Ballarotta, M. *et al.* On the resolutions of ocean altimetry maps. *Ocean Science* **15**, 1091–1109 (2019).

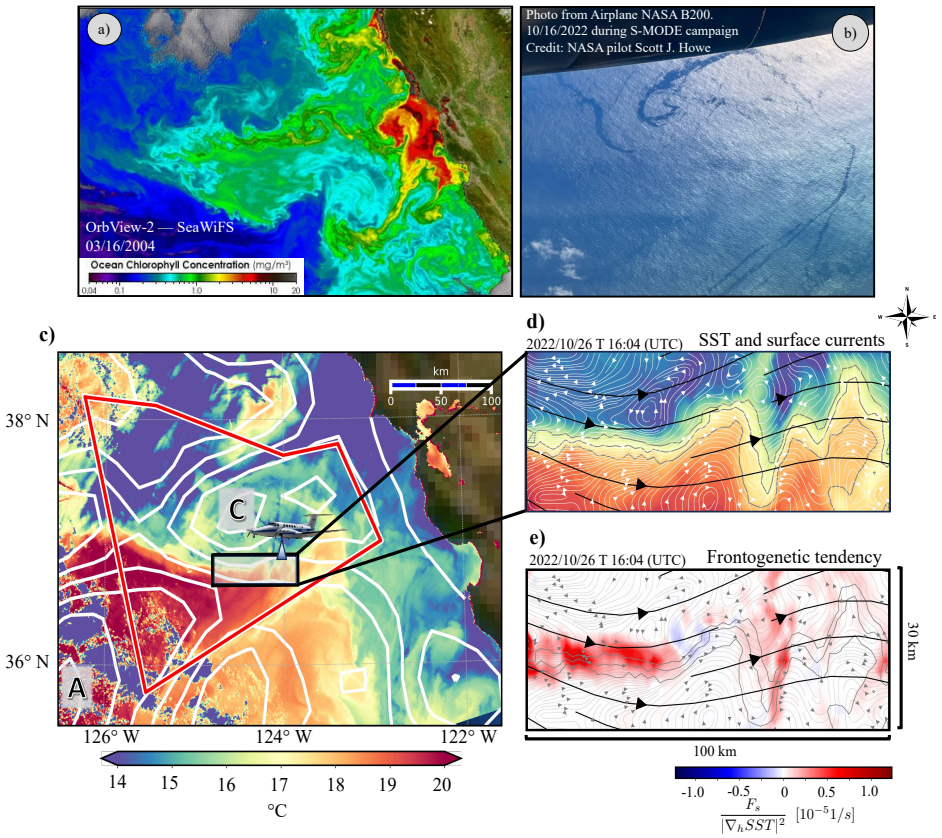
[35] Rio, M.-H. *et al.* Improving the altimeter-derived surface currents using high-resolution sea surface temperature data: a feasability study based on model outputs. *Journal of Atmospheric and Oceanic Technology* **33**, 2769–2784 (2016).

[36] Rodríguez, E. *et al.* Ka-band doppler scatterometry over a loop current eddy. *Remote Sensing* **12**, 2388 (2020).

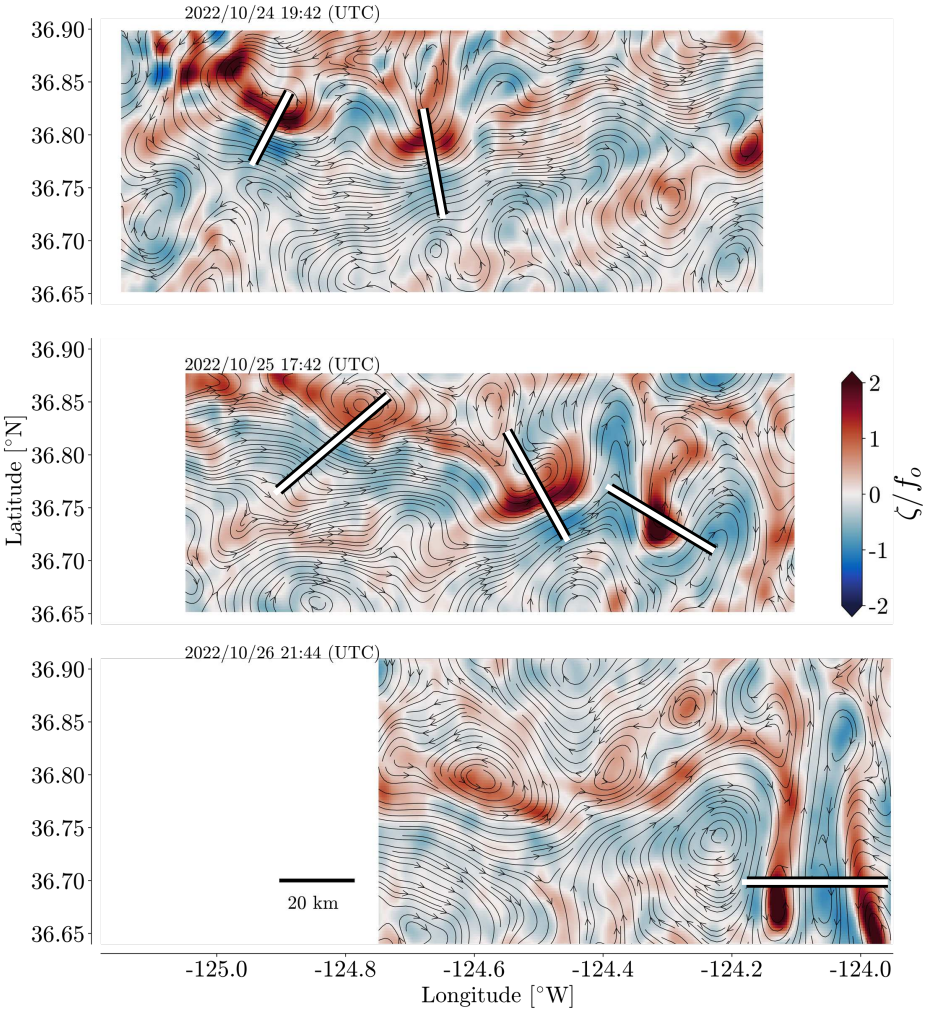
[37] Wineteer, A. *et al.* Measuring winds and currents with ka-band doppler scatterometry: An airborne implementation and progress towards a spaceborne mission. *Remote Sensing* **12**, 1021 (2020).

[38] Vallis, G. K. *Atmospheric and oceanic fluid dynamics* (Cambridge University Press, 2017).

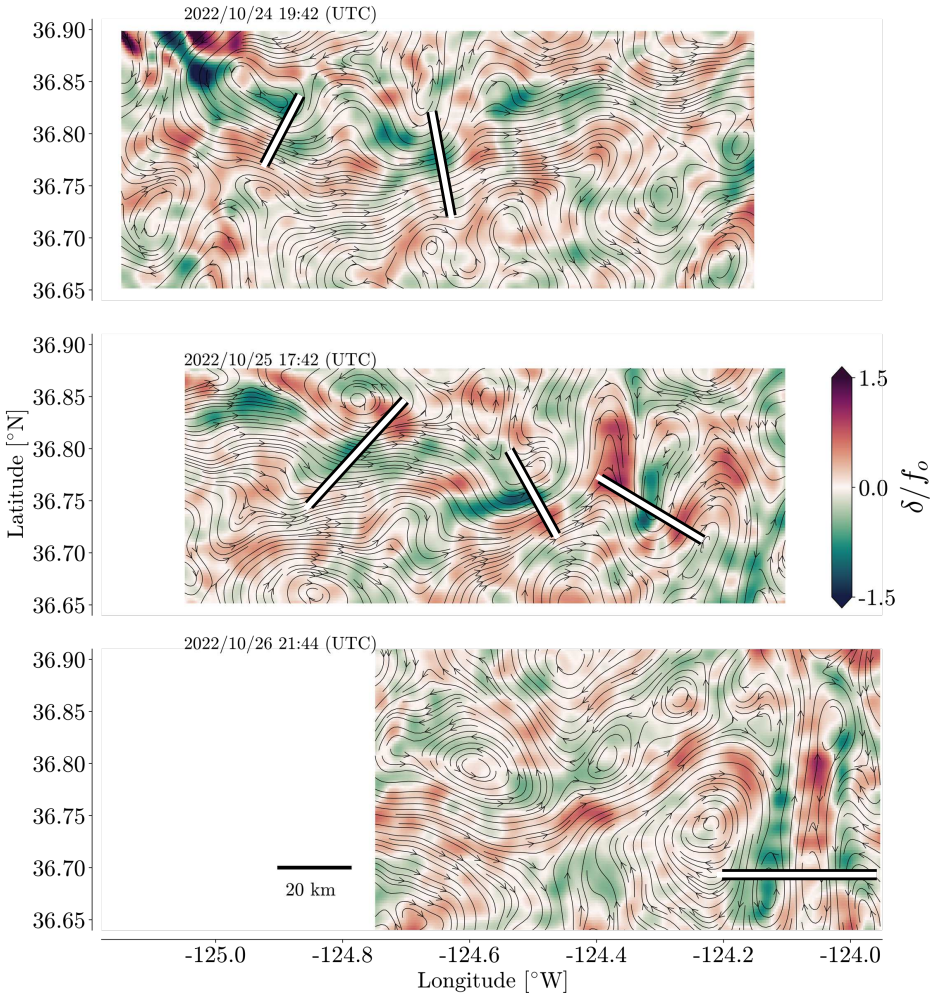
[39] Molemaker, M. J., McWilliams, J. C. & Capet, X. Balanced and unbalanced routes to dissipation in an equilibrated eady flow. *Journal of Fluid Mechanics* **654**, 35–63 (2010).



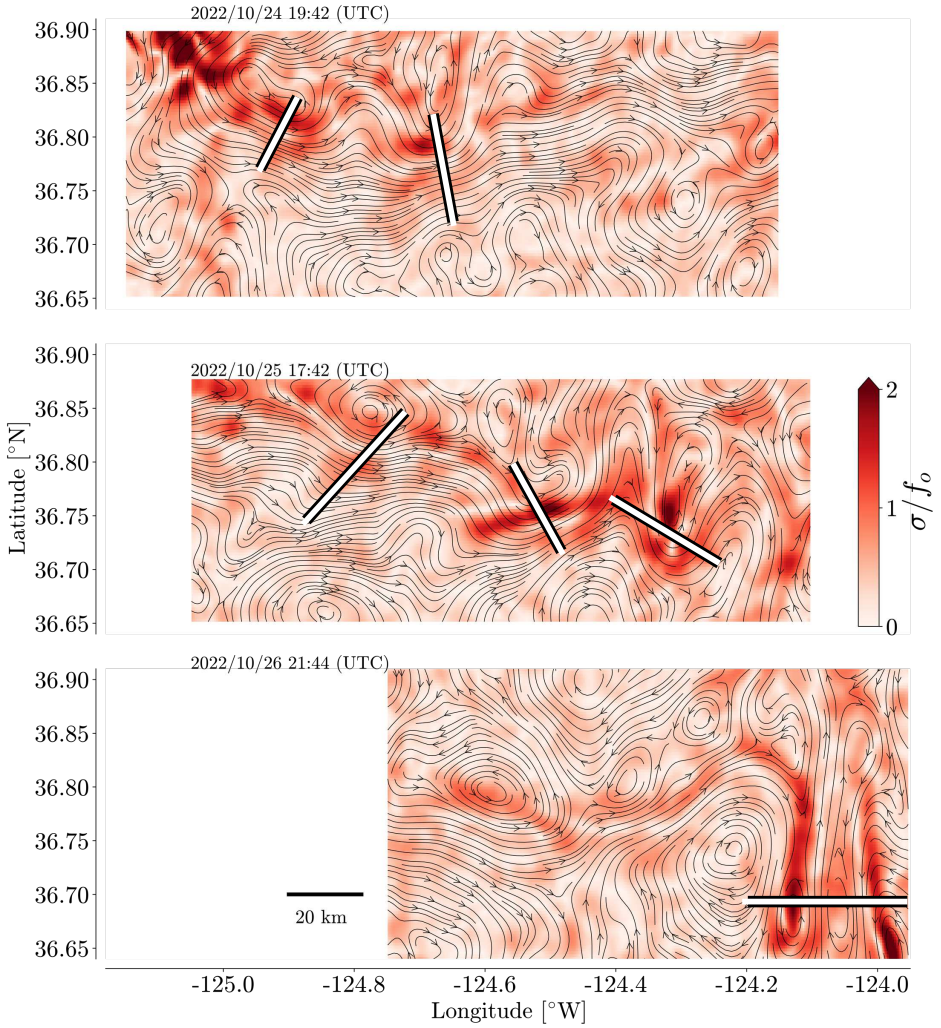
Extended Data Figure 1. A multiscale view of the ocean. a) Chlorophyll concentration from satellite. b) Photograph taken from the NASA King Air B200 aircraft at an altitude of 28,000 ft during S-MODE campaign in October 16, 2022. c) Sea surface temperature (SST) from the VIIRS satellite (colormap in (c)) and geostrophic flow from satellite altimeters (see Methods) (white contours in (c) and black contours in (d, e)). The capital letters A and C in panel (c) stand for anticyclonic eddy and cyclonic eddy, respectively. The red polygon in panel (c) marks the S-MODE region (Methods). The black rectangle in panel (c) identifies the 100-km by 30 km area sampled by DopplerScatt. d) shows high-resolution SST (color) measured simultaneously with DopplerScatt from the same aircraft and the streamlines (white contours) of the rotational component of the high-pass DopplerScatt velocities. Thick gray contours are the 17.0,17.5,18.0 °C isotherms. e) Frontogenetic tendency (eq.3) computed from satellite VIIRS SST and the DopplerScatt high-pass velocity gradients (< 15 km).



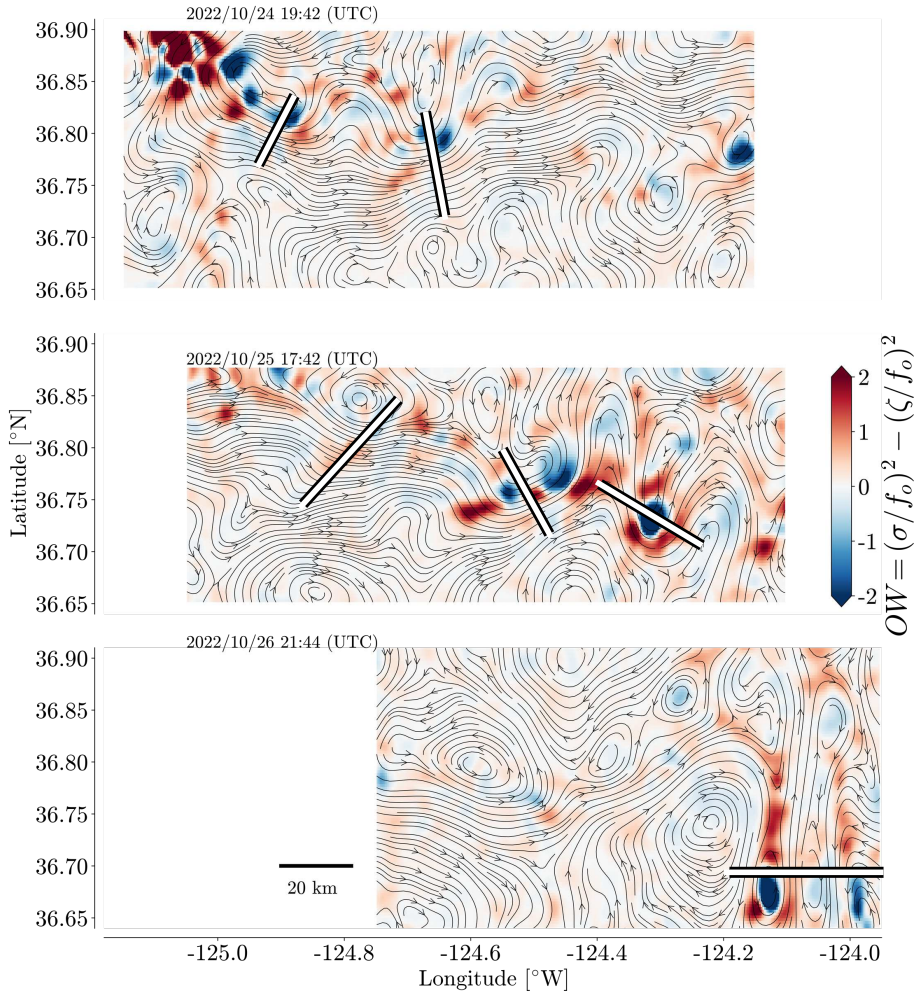
Extended Data Figure 2. Spatio-temporal evolution of submesoscale relative vorticity field deformation normalized by Coriolis parameter f_o. The white lines mark the location of dipole structures.



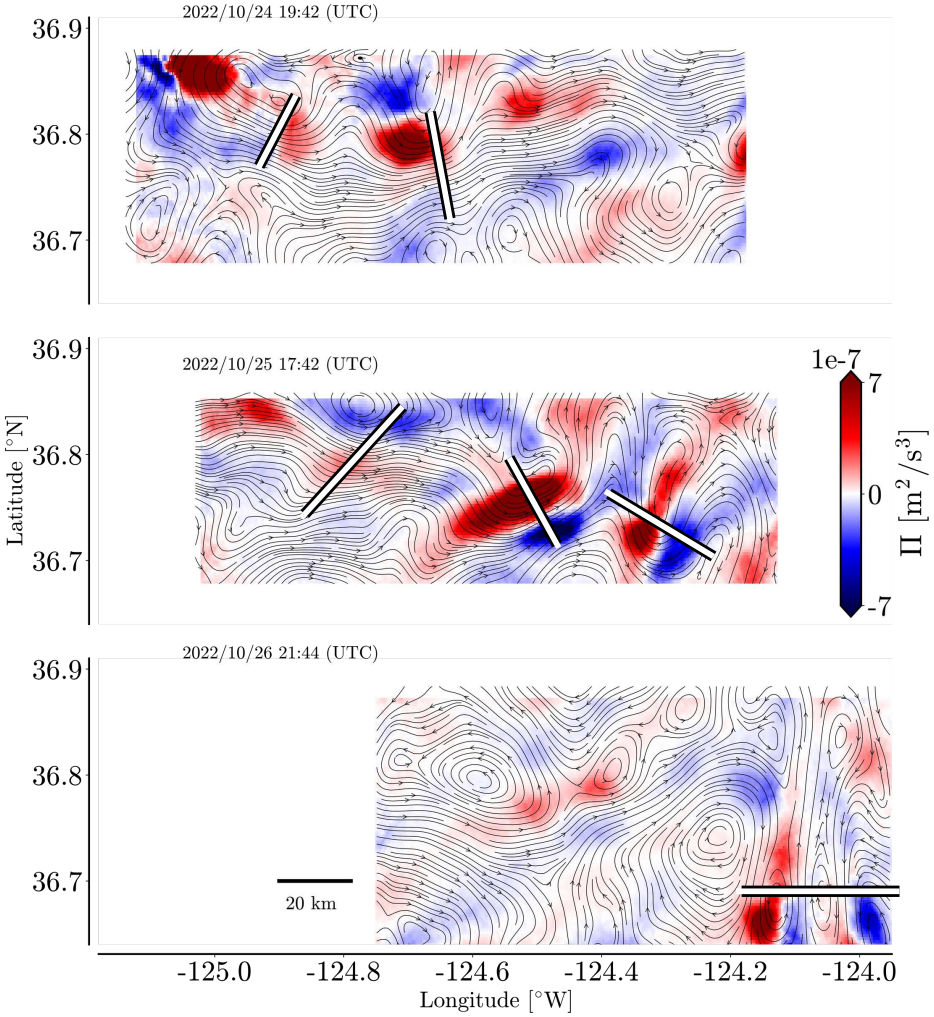
Extended Data Figure 3. Spatio-temporal evolution of submesoscale divergence field deformation normalized by Coriolis parameter f_o. The white lines mark the location of dipole structures.



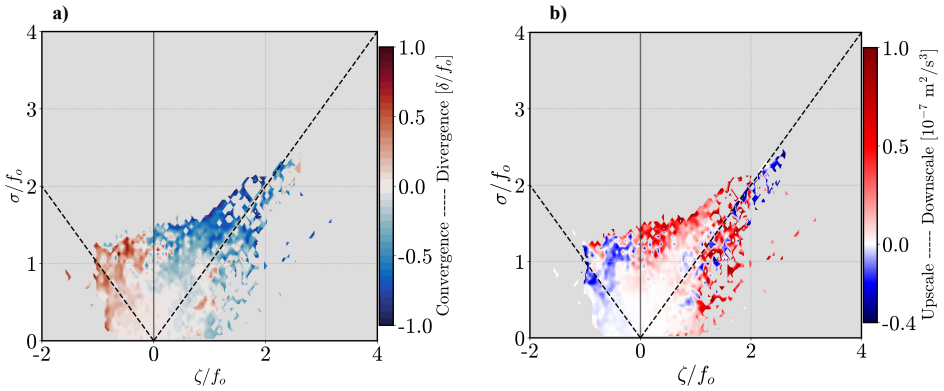
Extended Data Figure 4. Spatio-temporal evolution of submesoscale strain field deformation normalized by Coriolis parameter f_o. The white lines mark the location of dipole structures.



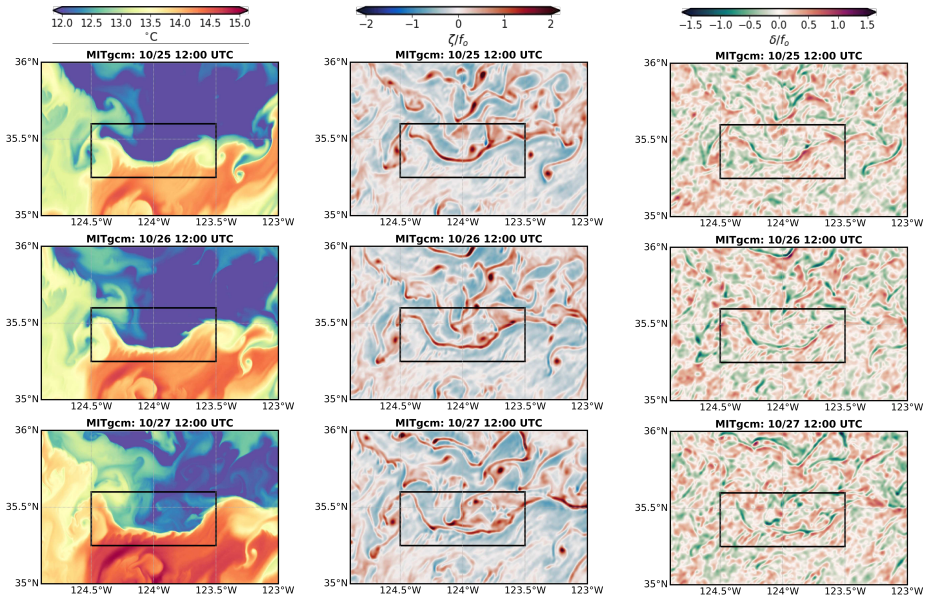
Extended Data Figure 5. Spatio-temporal evolution of Okubo-Weiss parameter normalized by Coriolis parameter f_o. The white lines mark the location of dipole structures.



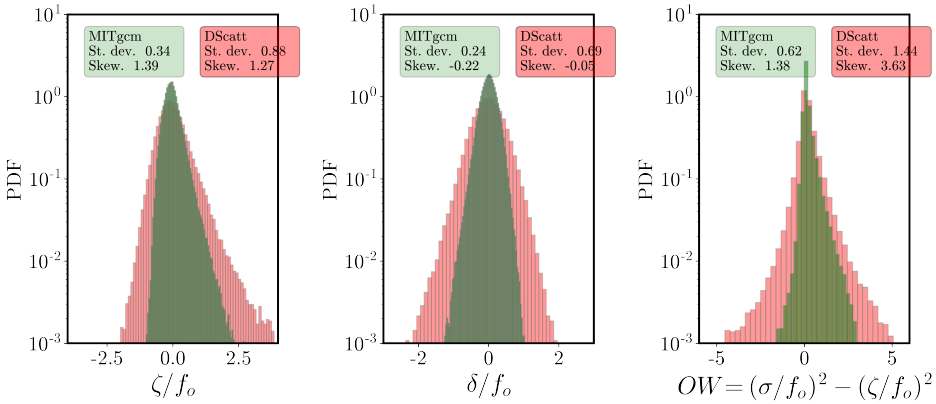
Extended Data Figure 6. Spatio-temporal evolution of surface cross-scale kinetic energy flux Π at 5 km computed with the coarse-graining method. The white lines mark the location of dipole structures: vorticity and KE fluxes anti-correlated with divergence.



Extended Data Figure 7. Divergence and cross-scale kinetic energy flux Π (at 5-km scale) in the vorticity-strain space. The distribution in both panels is based on four consecutive flights. Black dashed 45° lines correspond to a shear flow $\sigma = |\zeta|$ [3].



Extended Data Figure 8. Time evolution of a frontal system from numerical ocean model. Surface fields of SST, surface relative vorticity, and divergence from high-resolution ocean numerical model smoothed at 2-km. The black rectangle shows the size of the domain covered by DopplerScatt during S-MODE campaign. Note that is not in the same location, but the size is the same.



Extended Data Figure 9. Statistics of submesoscale kinematics from MITgcm ocean general circulation model and DopplerScatt. Probability density histograms of surface relative vorticity (left panel), divergence (right panel) normalized by the Coriolis frequency f_o, and Okubo-Weiss quantity (third). Green shading is the statistics from high-resolution MITgcm simulation (spacing grid of 500 m) smoothed at 2-km and pink shading is the statistics from DopplerScatt smoothed at 2-km. Both statistics are based upon daily snapshots over 4 days and considering the whole domain shown in Extended Data Figure 8.

Supplementary Files

This is a list of supplementary files associated with this preprint. Click to download.

- SMODEDScattSIMay2024.pdf